Croatian Society for Materials Protection

Metalurgija/Metallurgy

Vol. 66 No. 2 / 2027

Numerical Simulation and Process Optimization of Backward Extrusion for 7A60 Aluminum Alloy Tubes

Ning Wang [1,2], Ruijue Wang [3], Tizhuo Jia [1,2], Shuangyong Tian [1,2], Zhen Xu [1,2*], Sai Li [1,2*] and Chengning Li [4]

https://doi.org/10.64486/m.66.2.9

[1] School of Material and Metallurgy, University of Science and Technology Liaoning, Anshan 114051, Liaoning, China
[2] The key Laboratory of material Forming and Structure Property control, Anshan 114051, Liaoning, China
[3] Hexing Aeronautical Materials (Tianjin) Technology Co., Ltd., Tianjin 300399, China
[4] School of Materials Science and Engineering, Tianjin University, Tianjin, 300350, China
* Correspondence: e-mail: ustlxuzhen@126.com; (Z. X); 322020@ustl.edu.cn (S. L)

Type of the Paper: Article
Received: July 1, 2026
Accepted: September 4, 2026

Abstract: 7A60 ultra-high-strength aluminum alloy seamless tubes are key components in lightweight structural applications, but their backward extrusion poses significant challenges due to the narrow processing window and high deformation resistance. Through numerical simulation and experimental validation, the effects of extrusion temperature (360–450) °C and speed (0.1–5) mm/s on load, temperature field, stress, and strain were investigated. Results indicate that raising temperature reduces deformation resistance, yet excessive heating at the die exit promotes hot cracking; speeds ≥3 mm/s raise the exit temperature to (492–516) °C, exceeding the solidus and deteriorating forming quality. The optimized conditions are 390 °C and 0.5 mm/s, which give the most uniform strain distribution. Extruded tubes exhibit a layered structure from surface to center: fine-grained zone, mixed-grain zone, and fibrous structure. The area fraction of secondary phases decreases from 5.5 % in the as-cast state to (3.4–4.9) % in the as-extruded state, depending on the sampling position. Mechanical properties are significantly improved after extrusion, with ultimate tensile strength, yield strength, and elongation reaching 426.8 MPa, 272 MPa, and 14.0 %, respectively.

Keywords: aluminum alloy; tube; backward extrusion; numerical simulation

1. Introduction

With the rapid advancement of modern industrial technology, aluminum alloy materials have been widely used in fields such as aerospace equipment, intelligent automobile manufacturing, and new building structures due to their low density, high strength, excellent corrosion resistance, and good processing adaptability [1-3]. Among these, aluminum alloy seamless tubes have become the ideal material for key load-bearing structural components because of their uniform microstructure, absence of weld defects, and excellent compressive and fatigue resistance [4-5]. Currently, the forming of aluminum alloy seamless tubes primarily employs two processes: forward extrusion and backward extrusion. In comparison, during the backward extrusion process, the billet moves synchronously with the extrusion container, resulting in no relative friction between them. This offers significant advantages such as lower extrusion force, high product dimensional accuracy, superior forming quality, uniform mechanical properties, and high extrusion efficiency [6-7].

https://doi.org/10.64486/m.66.2.9

During the extrusion process of aluminum alloy seamless tubes, the extrusion temperature and extrusion speed are key process parameters that influence material flow behavior and the final forming quality. Due to the high cost and long cycle of experimental research, as well as the difficulty in obtaining the dynamic evolution of the temperature field, stress field, and strain field in real time and accurately during the extrusion process [8], Li et al. [9] systematically investigated the effects of forming temperature and extrusion speed on the forming quality of 7075 aluminum alloy seamless tubes. They pointed out that temperatures that are too low or too high increase the tensile stress in the exit zone, while an increase in extrusion speed reduces the uniformity of metal flow. Zhang et al. [10] analyzed the influence of extrusion temperature and speed on the extrusion force, temperature field, and stress distribution during the extrusion of 7075 aluminum alloy seamless tubes through numerical simulation. Ketabchi et al. [11] studied the deformation behavior of 7075 aluminum alloy during backward extrusion by combining experiments with the finite element method, finding significant inhomogeneity in the distribution of effective stress and strain within the deformed billet. Neag et al. [12] explored the thixoextrusion behavior of 7075 aluminum alloy under different temperature conditions based on numerical simulation. It is evident that conducting numerical simulation research on the extrusion process based on actual working conditions holds significant theoretical significance and engineering value for revealing the deformation behavior of materials under thermal-mechanical coupling. However, research on the numerical simulation and systematic process parameter optimization for the backward extrusion forming of 7A60 ultra-high-strength aluminum alloy seamless tubes is still relatively limited. Therefore, carrying out research on the numerical simulation and process optimization of the backward extrusion process for 7A60 aluminum alloy tubes is of great practical importance.

Therefore, this paper employs numerical simulation methods to systematically investigate the effects of extrusion temperature and extrusion speed on the load-stroke curve, temperature field, equivalent stress, and equivalent strain distribution during the backward extrusion process of 7A60 aluminum alloy tubes. Based on this, the key process parameters are optimized, and finally, the simulation results are validated through extrusion experiments. The research findings can provide a theoretical basis and engineering reference for the preparation of 7A60 ultra-high-strength aluminum alloy seamless tubes, and are of significant engineering value for improving the forming quality and application performance of 7000 series aluminum alloys in key load-bearing structural components.

2. Materials and Methods

2.1. Materials and Properties

The material used in both the simulation and experiments was 7A60 aluminum alloy, and its chemical composition is presented in Table 1. The materials used for the extrusion container, die, and pad during the extrusion process were all H13 tool steel. The material properties of the 7A60 aluminum alloy and H13 tool steel are shown in Table 2 [13].

Table 1. Chemical composition of 7A60 aluminum alloy (mass fraction / %)

Zn	Mg	Cu	Zr	Fe_{max}	Si_{max}	Mn_{max}	Cr_{max}	Ti	Al
8.0-9.0	2.3-3.0	2.0-2.6	0.1-0.2	0.25	0.12	0.1	0.05	0.02-0.03	Bal.

Table 2. Material properties of 7A60 aluminum alloy and H13 tool steel

	Density $kg \cdot m^{-3}$	Specific Heat Capacity / $J \cdot (kg \cdot K)^{-1}$	Thermal Conductivity / $W \cdot (m \cdot K)^{-1}$	Coefficient of Thermal Expansion / K^{-1}	Young's Modulus MPa	Poisson's Ratio
7A60	2850	960	130	0.0000236	71000	0.33
H13	7870	460	24.3	-	210000	0.35

https://doi.org/10.64486/m.66.2.9

The flow stress of the 7A60 aluminum alloy at elevated temperatures used in the numerical simulations is described by the Arrhenius-type constitutive equation derived from isothermal hot compression tests on the same alloy grade [14]:

$$\dot{\epsilon} = 9.84 \times 10^{36}[sinh(0.004814\sigma)]^{9.7456} exp\left[-\frac{4.38981 \times 10^5}{RT}\right] \quad (1)$$

where $\dot{\epsilon}$ is the strain rate (s^{-1}), σ is the flow stress (MPa), R is the gas constant (8.314 $J \cdot mol^{-1} \cdot K^{-1}$), and T is the absolute temperature (K). The constitutive parameters include the thermal activation energy Q of 438.981 kJ/mol, the stress exponent n of 9.7456, the stress level parameter α of 0.004814 MPa^{-1}, and the structure factor A of 9.84×10^{36} s^{-1}. This model shows a fitting accuracy of 99.7 % for the present alloy.

2.2. Numerical Model Setup

The numerical simulation of the backward extrusion process for the 7A60 aluminum alloy tube was conducted using the finite element analysis software DEFORM V11.0 3D. The extrusion billet had an outer diameter of 272 mm, an inner diameter of 142 mm, and a height of 300 mm. The target tube had an outer diameter of 155 mm and an inner diameter of 143 mm. First, three-dimensional solid models of the billet, punch, and die were established using SolidWorks software, as shown in Figure 1(a). Considering the symmetry of the geometry and boundary conditions, a quarter model was adopted for simplified analysis. The billet was constructed as a quarter-solid with an inner hole at a 1:1 scale, while the dies were set as rigid bodies to improve computational efficiency, as illustrated in Figure 1(b)(c). Subsequently, the 3D models were assembled and pre-processed. To determine the influence of extrusion temperature and extrusion speed on the load-stroke curve, temperature field, equivalent stress, and strain distribution during the extrusion process of the 7A60 aluminum alloy tube, the boundary conditions were set as shown in Table 3.

The numerical simulation employs a rigid-plastic material model with the following fundamental assumptions: (1) elastic deformation is neglected; (2) body forces and inertial effects are ignored; (3) the material follows the Levy–Mises constitutive equations; (4) the material is isotropic and homogeneous; (5) the volume remains constant during deformation; and (6) loading conditions define the boundary between rigid and plastic regions. The billet was discretized using 100,000 tetrahedral elements (23,862 nodes) with a minimum element size of 1.87 mm. A shear friction model was applied with a friction coefficient of 0.3. The heat transfer coefficient between the billet and the die was set to 5 N/(mm • s • °C), and that between the billet and the ambient air was 0.02 N/(mm • s • °C). The ambient temperature was fixed at 20 °C.

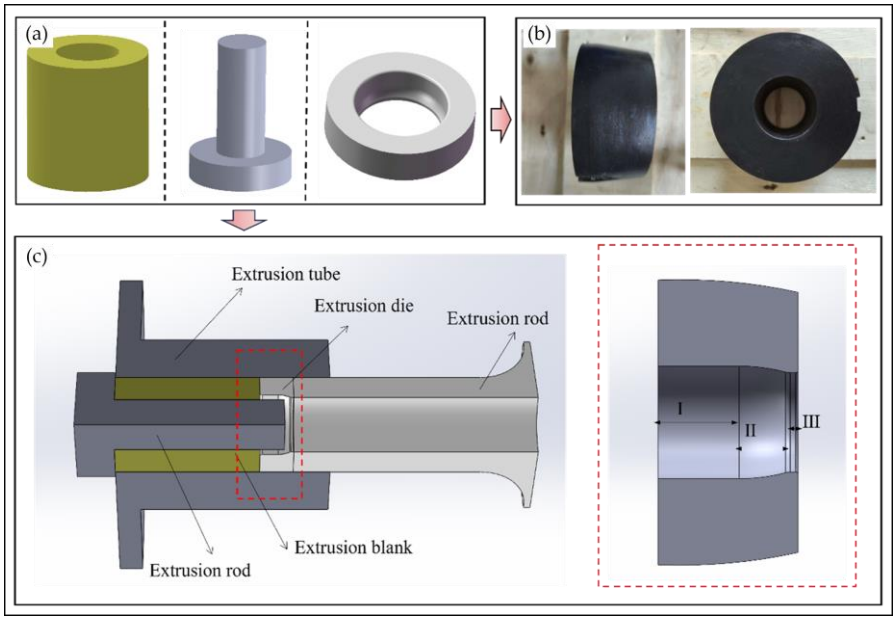


Figure 1. (a) Models of the billet, punch, and die; (b) Extrusion die; (c) Quarter extrusion model

https://doi.org/10.64486/m.66.2.9

Table 3. Boundary conditions and process parameters

Parameters	Value
Billet and die preheating temperature / °C	360, 390, 420, 450
Extrusion speed / (mm/s)	0.1, 0.5, 1, 3, 5
Heat transfer coefficient between billet and die / N/(mm·s·°C)	5
Heat transfer coefficient between billet and air / N/(mm·s·°C)	0.02
Friction type	Shear friction
Friction coefficient	0.3
Ambient temperature / °C	20

2.3. Backward Extrusion Experiments and Characterization

First, the 7A60 aluminum alloy ingot was subjected to a two-stage homogenization treatment in a vacuum heating furnace. The heating rate of the furnace was set to 10 °C/min until reaching 460 °C. The ingot was placed in the furnace and held at this temperature for 1 h. Subsequently, the temperature was increased to 470 °C within 10 min and held for 24 h, followed by cooling to room temperature. After homogenization, the aluminum alloy material was machined to obtain specimens of the required dimensions for extrusion. Finally, the extrusion billet was heated and then placed into the extrusion container of a 2500 t backward extrusion press for the backward extrusion experiment, producing a 7A60 aluminum alloy tube with an outer diameter of 155 mm and a wall thickness of 6 mm. The extruded tube was then air-cooled to room temperature.

Differential scanning calorimetry (DSC) analysis was performed on a Setaram Setsys Evolution instrument from 25 °C to 750 °C at a heating rate of 10 °C/min under an argon atmosphere. The DSC curve was used to determine the solidus temperature of the 7A60 aluminum alloy. Metallographic structures under polarized light were observed using a Polyvar-MET metallurgical microscope. The sampling positions are shown in Figure 2(a)(b), and the specimen dimensions were 10 mm × 6 mm × 5 mm. The average grain sizes of the as-cast and homogenized alloys were determined from polarized light optical micrographs using the linear intercept method in accordance with ASTM E112-13. For each condition, five representative micrographs were analyzed at a magnification of ×200. On each micrograph, three horizontal and three vertical lines were drawn, and the number of grain boundaries intersecting each line was counted. The average grain size was calculated from the total line length divided by the total number of intercepts. The reported values represent the average of the five measurements.

Semi-quantitative phase analysis of the aluminum alloy tube was conducted using an X'Pert X-ray diffractometer from Malvern Panalytical (UK), with a diffraction angle scanning range of 10° to 90° and a scanning speed of 10°/min. A Zeiss Gemini Sigma 300 VP high-resolution field emission scanning electron microscope (SEM) was used to observe the microstructure, particularly analyzing the size, distribution, and composition of secondary phases. The area fraction of secondary phases was determined from SEM images using Image-Pro Plus software. For each condition, including the as-cast, homogenized, and extruded states (inner side, central part, and outer side), five representative images were captured at a magnification of ×1000 from different fields of view. The secondary phase particles were distinguished from the aluminum matrix based on their contrast in the SEM images, and the area fraction was calculated as the ratio of the secondary phase area to the total analyzed area. The reported value for each condition represents the average of the five measurements. The standard deviation did not exceed 0.3 percentage points for any condition, indicating good reproducibility of the measurements. Room-temperature quasi-static tensile tests were performed using a UTM5305 electronic universal testing machine according to the GB/T228.1-2021 standard, with a tensile rate of 1.5 mm/s. The tensile specimens were cut along the extrusion direction. The specimen dimensions are shown in Figure 2(c). For each set of process parameters, three specimens from different locations were tested repeatedly, and the average of the three test results was taken as the final mechanical property data (ultimate tensile strength, yield strength, and elongation).

https://doi.org/10.64486/m.66.2.9

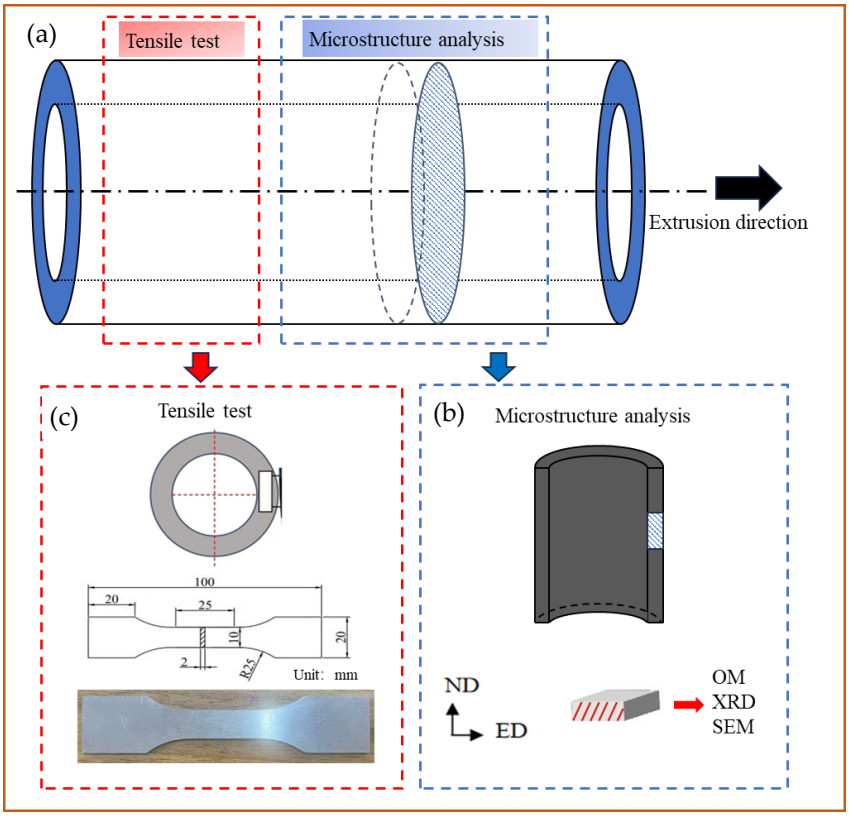


Figure 2. (a) Schematic diagram of the 7A60 aluminum alloy tube; (b) Sampling positions for testing; (c) Tensile specimen and actual sample

3. Results and discussion

Figure 3 shows the forming load-stroke curves of the 7A60 aluminum alloy tube at different extrusion temperatures. As can be seen from Figure 3, during the initial extrusion stage (0–t_1), the forming load remains near zero with slight fluctuations. This is mainly attributed to the fact that the aluminum alloy billet has not yet undergone substantial plastic deformation (as shown in Figure 4a), and the load at this stage primarily originates from the static friction between the billet and the inner wall of the extrusion container as well as the surface of the extrusion mandrel. When the extrusion progresses to time t_1, the process enters the upsetting-filling stage (t_1–t_3), as illustrated in Figure 4(b–c). The billet begins to undergo plastic flow and gradually fills the die cavity, with the forming load showing an approximately linear upward trend. The load increase during this stage mainly results from the work hardening behavior induced by severe plastic deformation of the material under constrained conditions. During the t_2–t_3 stage, the load decreases to some extent, indicating a transition period: at time t_2, the material begins to pre-extrude and flow into the die, accompanied by localized temperature rise, leading to a gradual decrease in extrusion force; this trend continues until time t_3 (as shown in Figure 4d). Thereafter, the material enters the formal extrusion state, undergoing significant plastic deformation, and the load increases rapidly. After the stroke reaches the critical point t_4, the process enters the steady-state extrusion stage (from t_4 to the end), as shown in Figure 4(e). The load curve fluctuates around a certain mean value, reflecting the alternating effects of work hardening and dynamic softening processes. This indicates that under high-temperature and large-deformation conditions, a dynamic equilibrium is achieved between work hardening and the softening effect induced by dynamic recrystallization. At this point, the extrusion process of the 7A60 aluminum alloy enters the basic extrusion stage, namely the steady-state flow stage.

Furthermore, it can also be observed from Figure 3 that under constant extrusion speed conditions, the extrusion force decreases systematically with increasing extrusion temperature. At extrusion temperatures of 360 °C, 390 °C, 420 °C, and 450 °C, the average extrusion forces during the steady-state extrusion stage are

https://doi.org/10.64486/m.66.2.9

7.01×10³ kN, 6.48×10³ kN, 6.02×10³ kN, and 5.33×10³ kN, respectively. When the extrusion temperature increases from 360°C to 450°C, the average load during the steady-state stage decreases by approximately 24.0 %. This trend is mainly attributed to the fact that, at a constant extrusion speed, an increase in temperature reduces the resistance to dislocation motion, lowers the yield strength of the material, and simultaneously enhances the dynamic softening effect, thereby significantly reducing the deformation resistance [15]. Therefore, from the perspective of reducing extrusion force, increasing the extrusion temperature has a positive effect. However, excessively high temperatures can lead to the accumulation of deformation heat and frictional heat in the metal, causing the billet temperature to become too high and potentially even inducing solid-liquid transformation of the material at the die exit, increasing the risk of fracture. Simultaneously, excessively high extrusion temperatures may also induce defects such as cracks and peeling on the product surface, adversely affecting the forming quality.

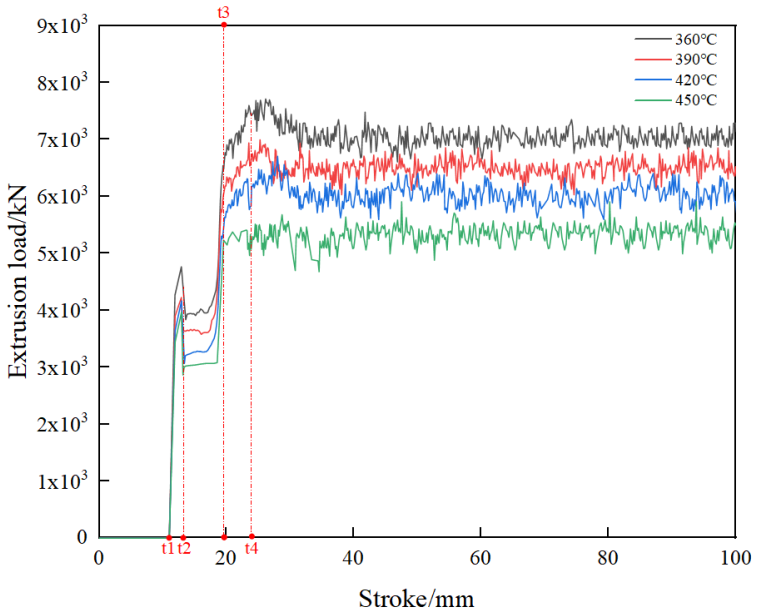


Figure 3. Extrusion load–extrusion stroke curve under different temperatures

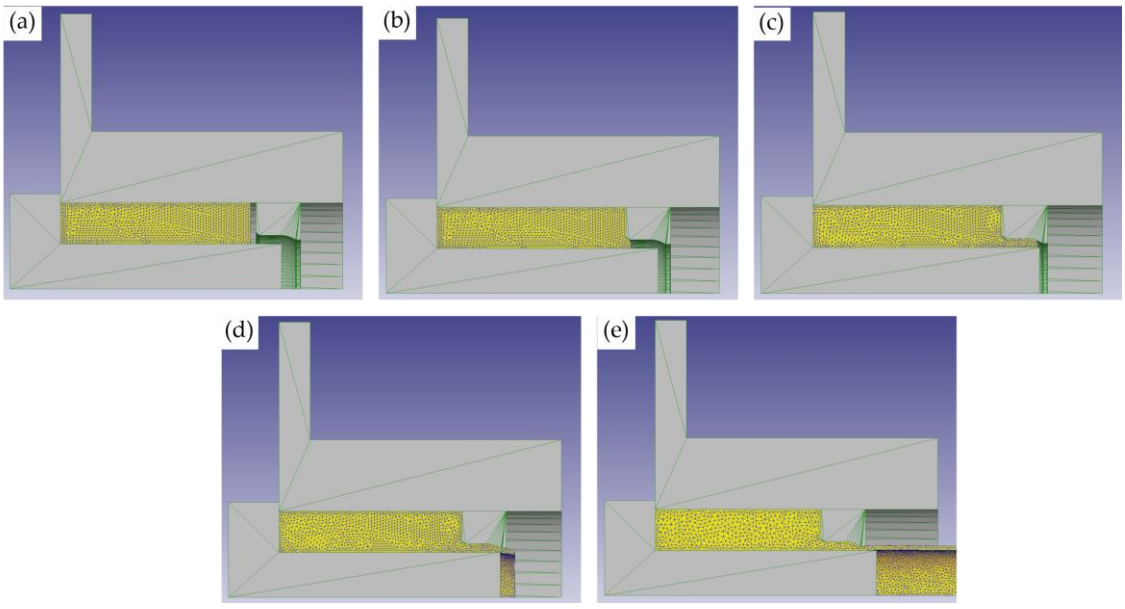


Figure 4. Schematic diagram of the aluminum alloy tube extrusion process: (a) initial stage; (b), (c) upsetting stage; (d) initial extrusion stage; (e) steady-state extrusion stage

https://doi.org/10.64486/m.66.2.9

Figure 5 shows the internal temperature field distribution of the aluminum alloy billet after extrusion forming at different extrusion temperatures. It can be observed from Figure 5 that after extrusion deformation, the entire billet exhibited varying degrees of temperature increase. This temperature rise mainly originated from two sources of heat contribution: one was the deformation heat generated by the severe plastic deformation of the aluminum alloy within the die cavity; the other was the frictional heat caused by the relative motion between the billet and the extrusion die.

Notably, because the die exit is the region where the billet undergoes the most severe deformation, the temperature increase in this area was the most significant. When the initial extrusion temperature was 360 °C, the temperature at the die exit region rose to 410 °C, a temperature increase of approximately 50 °C. When the initial extrusion temperature was 390 °C, the temperature at the die exit region rose to 414 °C, an increase of about 24 °C. When the initial extrusion temperature was 420 °C, the temperature at the die exit region reached 443 °C, an increase of about 23 °C. When the initial extrusion temperature was 450 °C, the temperature at the die exit region reached 467 °C, an increase of about 17 °C. The magnitude of the temperature rise at the die exit region decreased as the initial extrusion temperature increased. This phenomenon can be attributed to the differences in the flow behavior of the material at different temperatures: in the lower temperature range (e.g., 360 °C), the plastic flow ability of the aluminum alloy is relatively poor, and the resistance to dislocation motion is greater, leading to higher deformation resistance. According to the thermodynamic theory of plastic deformation, higher deformation resistance implies an increase in the unit deformation work, and most of this deformation work is converted into heat. Therefore, more heat is generated during low-temperature extrusion, resulting in a greater temperature rise. As the initial temperature increases, the thermal activation effect of the material is enhanced, and softening mechanisms such as dynamic recrystallization are initiated, which reduces the flow stress during deformation and decreases the unit deformation work. Simultaneously, at high temperatures, the heat capacity of the material increases slightly, providing a certain buffering effect against the temperature rise. The combination of these two factors leads to the trend where the magnitude of the temperature rise gradually decreases with increasing initial temperature.

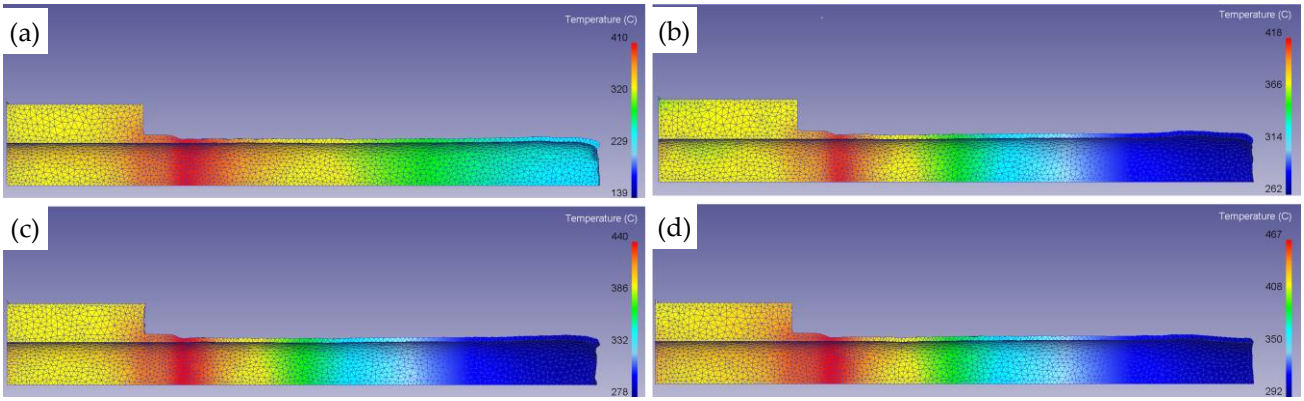


Figure 5. Effect of extrusion temperature on the temperature field inside the tube. (a) 360 °C; (b) 390 °C; (c) 420 °C; (d) 450 °C

Figure 6 shows the equivalent stress distribution contours of the 7A60 aluminum alloy tube at an extrusion speed of 0.5 mm/s and extrusion temperatures of 360 °C, 390 °C, 420 °C, and 450 °C. As the temperature increases, the stress in the undeformed region within the alloy generally shows a downward trend. This is mainly because, with the increase in extrusion temperature, the dynamic softening effect of the alloy becomes more pronounced, the deformation resistance of the alloy decreases, and the extrusion force required to extrude the tube is lower. As shown in Figures 6(a-d), when the preheating temperature is increased from 360 °C to 450 °C, the maximum equivalent stress significantly decreases from 137 MPa to 115 MPa, a reduction of 16.1 %. When the extruded tube begins to flow out of the die, it no longer contacts the die and is free from stress constraints. However, the calculated equivalent stress does not immediately drop to zero after the tube leaves the die; non-zero equivalent stress values remain in the simulated tube. Figures 6(e-h) show the equivalent

https://doi.org/10.64486/m.66.2.9

stress distribution contours of the extrusion billet. The stress value is relatively large on the inner wall side of the billet near the extrusion mandrel. This is mainly because, during the extrusion process, relative movement occurs between the billet and the extrusion mandrel, generating frictional force, which results in a relatively large stress value on the inner wall side of the billet metal.

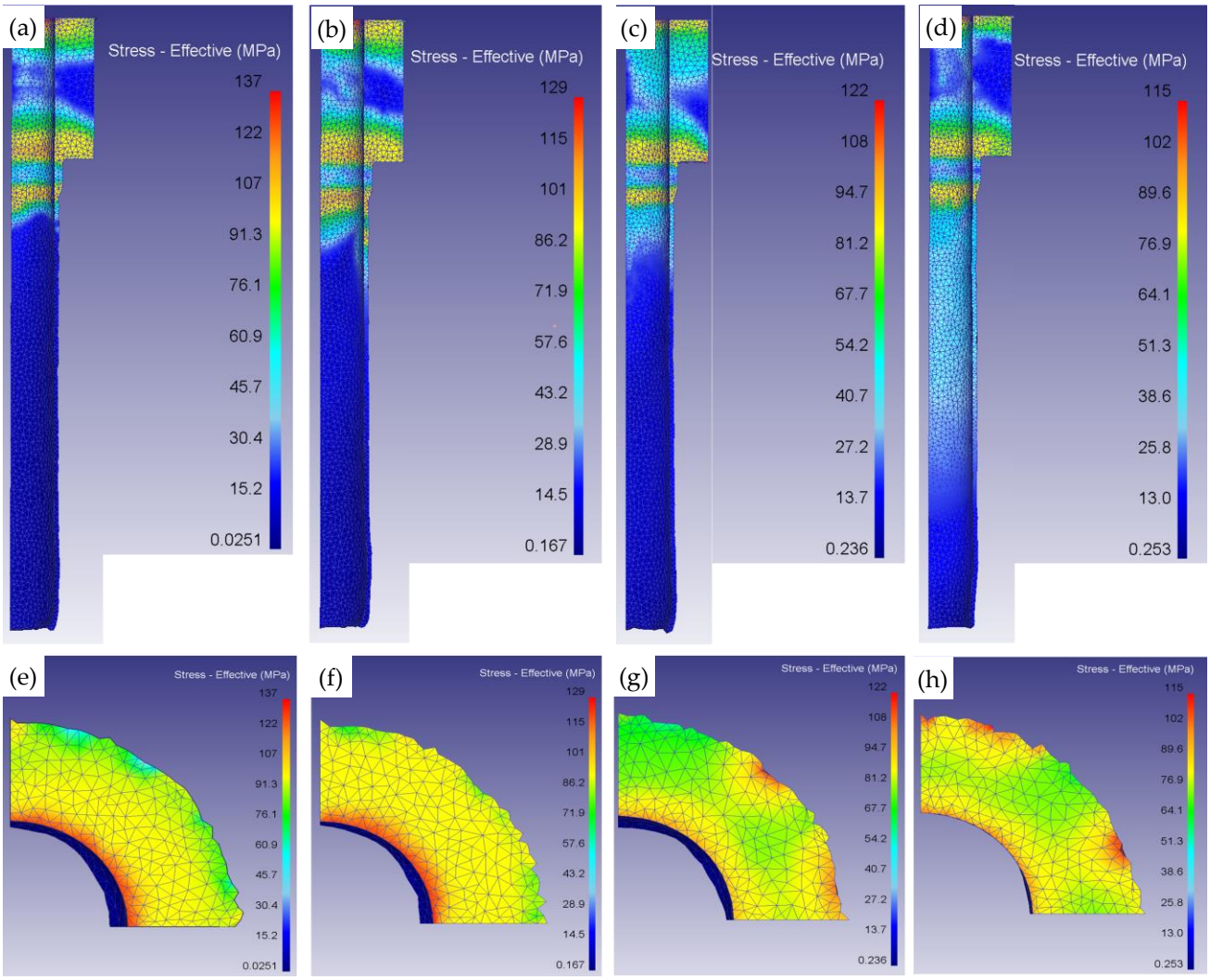


Figure 6. Effect of extrusion temperature on the equivalent stress of the tube and extrusion billet.
Tube: (a) 360 °C; (b) 390 °C; (c) 420 °C; (d) 450 °C
extrusion billet: (e) 360 °C; (f) 390 °C; (g) 420 °C; (h) 450 °C

Figure 7 presents the equivalent strain distribution contours inside the tube at different extrusion temperatures with a stroke of 80 mm. It can be observed from the figure that there is no significant difference in the overall distribution pattern and numerical range of the equivalent strain under different temperature conditions, indicating that the extrusion temperature has a relatively minor effect on the equivalent strain of the tube. This phenomenon can be attributed to the fact that the magnitude of the equivalent strain is primarily determined by process parameters such as the die geometry and extrusion ratio, while the influence of temperature is relatively limited. In the large deformation region, the equivalent strain on the outer side is significantly higher than that on the inner side due to the more severe plastic flow experienced by the outer material. However, in the billet region near the top of the mandrel, the strain accumulation on the inner wall side is greater than that on the outer side because of the relative sliding and resulting friction between the billet and the mandrel.

https://doi.org/10.64486/m.66.2.9

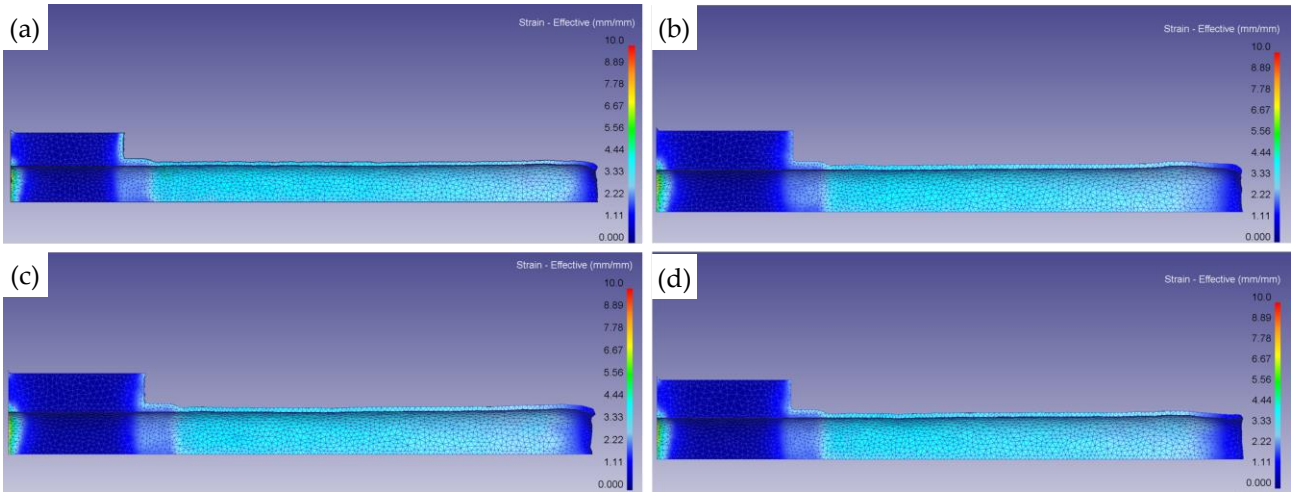


Figure 7. Effect of extrusion temperature on the equivalent strain of the tube. (a) 360 °C; (b) 390 °C; (c) 420 °C; (d) 450 °C

Figure 8 shows the distribution of equivalent strain and its deviation in the tube at different extrusion temperatures. From this figure, it can be seen that the change in extrusion temperature primarily affects the strain uniformity of the aluminum alloy tube. The effective strain deviation exhibits significant differences under different temperature conditions. Specifically, at an extrusion temperature of 390 °C, the average effective strain reaches its maximum value, while the effective strain deviation is at its minimum. This indicates that the material exhibits the most sufficient plastic flow and the best deformation uniformity under this temperature condition. In summary, it can be concluded that optimal forming performance is achieved at an extrusion temperature of 390 °C.

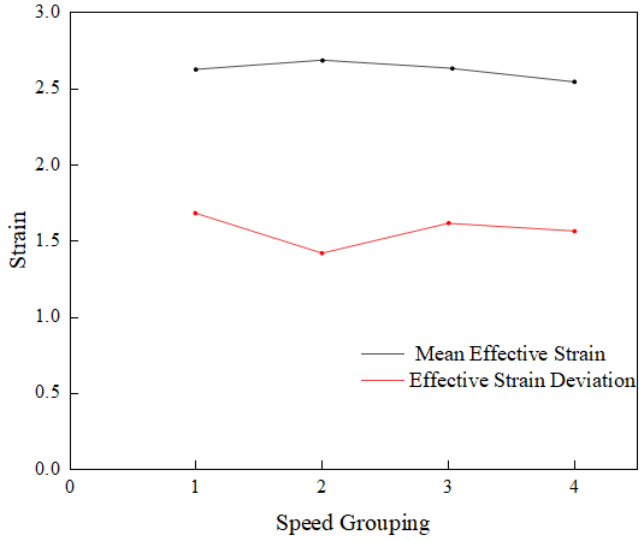


Figure 8. Equivalent strain and effective strain deviation at different extrusion temperatures

Figure 9 shows the temperature field distribution contours inside the tube at different extrusion speeds during the steady-state extrusion stage (extrusion stroke of 80 mm). It can be observed from Figure 9 that as the extrusion speed increases, the overall temperature of the tube rises significantly, with the most prominent temperature increase occurring in the die exit region. This phenomenon is mainly attributed to two factors: first, a higher extrusion speed intensifies the deformation rate of the metal, leading to a substantial increase in deformation heat generated per unit time; second, the increased extrusion speed shortens the time available for heat conduction and dissipation to the outside, causing heat to accumulate rapidly within the billet. As the die exit is the region with the most severe deformation, the heat input is most concentrated, resulting in the greatest temperature rise.

https://doi.org/10.64486/m.66.2.9

Specifically, when the extrusion speed is 0.1 mm/s (Figure 9a), the maximum internal temperature of the tube is only 318 °C. Under this condition, the temperature of 318 °C is significantly below the temperature range that enables adequate plastic flow for this alloy, resulting in insufficient plastic flow ability, high deformation resistance, and poor die filling. This not only leads to an increase in extrusion force and exacerbates die wear but also readily induces forming defects such as surface cracks, warping, and dimensional springback in the tube. When the extrusion speed is increased to 0.5 mm/s (Figure 9b), the temperature at the die exit rises to 414 °C, and the overall temperature distribution is relatively uniform. Yang Hongtao et al. [16] pointed out that the suitable extrusion temperature for 7A60 aluminum alloy should be controlled around 420 °C. This temperature window can both avoid low-temperature forming defects and effectively inhibit overheating damage, representing a critical process range for balancing forming quality and microstructure properties. However, when the extrusion speed is further increased to 3 mm/s and 5 mm/s (Figures 9d–e), the internal temperature of the tube rises sharply, with the die exit temperature reaching 492 °C and 516 °C, respectively, which exceed the solidus temperature of the 7A60 aluminum alloy (approximately 474 °C, as determined by the DSC analysis in the present study, Figure 9(f)). For Al-Zn-Mg-Cu series high-strength aluminum alloys, an excessively high extrusion speed causing the exit temperature to exceed the solidus line can induce defects such as a rough surface, scratches, and hot cracks in the product, and deteriorate the material's microstructure and mechanical properties [17,18].

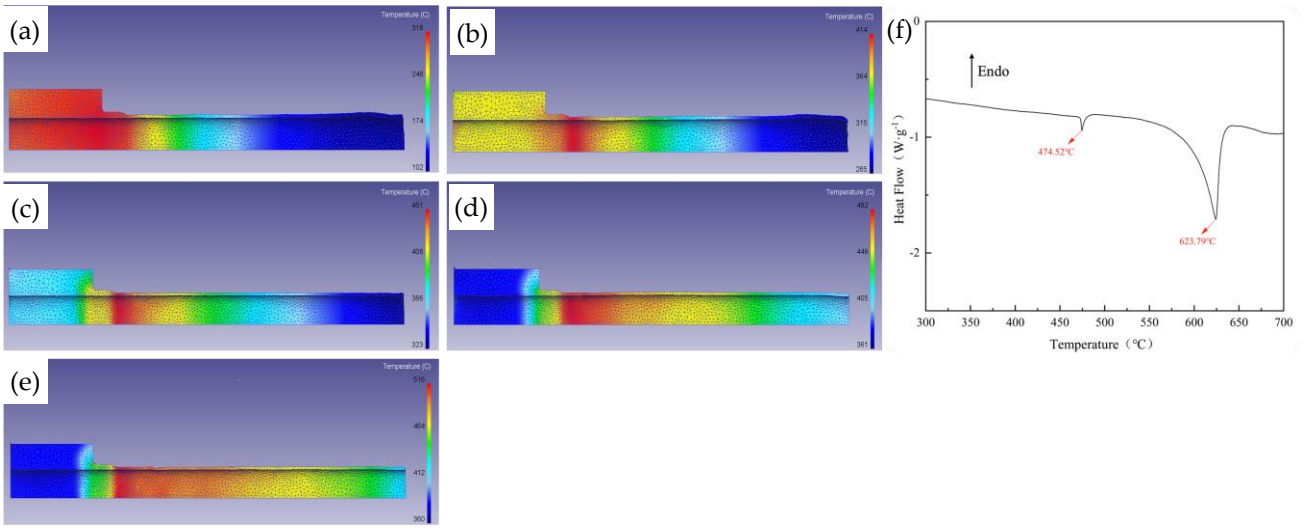


Figure 9. Effect of extrusion speed on the extrusion temperature field and DSC curve of the 7A60 aluminum alloy. (a) 0.1 mm/s; (b) 0.5 mm/s; (c) 1 mm/s; (d) 3 mm/s; (e) 5 mm/s; (f) DSC curve showing the solidus temperature

Figure 10 presents the equivalent stress distribution contours of the tube at different extrusion speeds during the steady-state extrusion stage (extrusion stroke of 80 mm). It can be observed from the figure that as the extrusion speed increases, the equivalent stress exhibits a distinct bimodal trend: first decreasing and then increasing. In the low-speed range (0.1–1) mm/s, the equivalent stress decreases from 158 MPa to 125 MPa. This is because the heat generated by plastic deformation accumulates with increasing deformation rate, enhancing the thermal softening effect to a degree that outweighs work hardening. The longer deformation time at these speeds allows more uniform heat conduction throughout the billet. In the high-speed range (1–5 mm/s), the equivalent stress rises again from 125 MPa to 145 MPa. Although the die-exit temperature can locally reach 492–516°C as shown in Figure 9, this temperature surge is confined to a thin surface layer near the exit. In the bulk deformation zone, the deformation time in the bulk zone is extremely short, as the material passes through the die exit region rapidly at high speeds, which severely limits heat diffusion. Consequently, work hardening driven by rapid dislocation multiplication outpaces thermal softening in the interior of the billet, leading to the observed increase in equivalent stress.

https://doi.org/10.64486/m.66.2.9

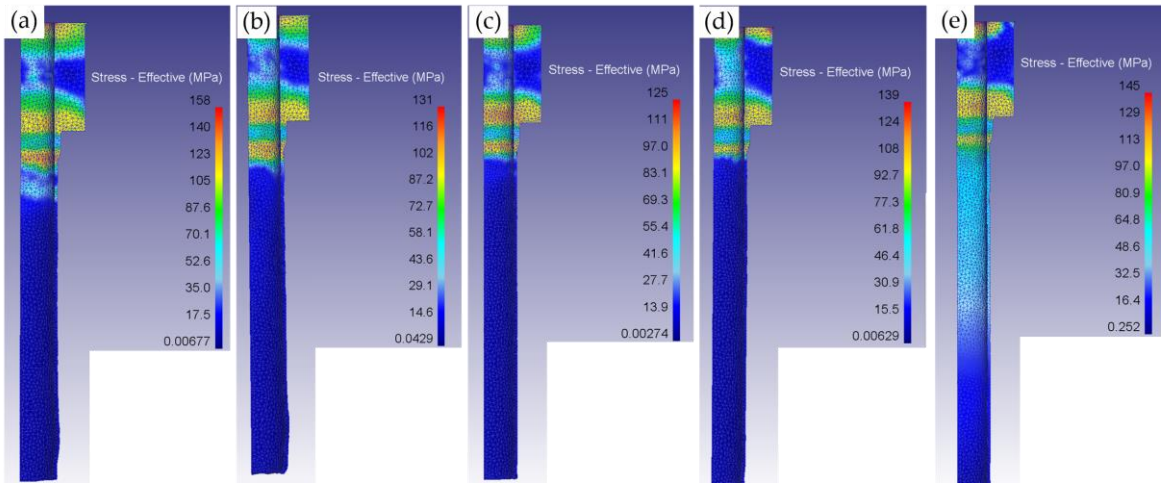


Figure 10. Effect of extrusion speed on extrusion equivalent stress
(a) 0.1 mm/s; (b) 0.5 mm/s; (c) 1 mm/s; (d) 3 mm/s; (e) 5 mm/s

Figure 11 shows the equivalent strain distribution contours of the tube at different extrusion speeds during the steady-state extrusion stage (extrusion stroke of 80 mm). From Figures 11(a-e), it can be observed that under different extrusion speed conditions, the overall equivalent strain values of the tube do not change significantly. Further observation of the equivalent strain distribution in the tube exit region shown in Figures 11(f–j) reveals that, at extrusion speeds above 0.5 mm/s, the uniformity of the equivalent strain generally decreases with increasing extrusion speed. Specifically, at extrusion speeds of 0.1 mm/s and 0.5 mm/s, the strain uniformity is significantly better than that at speeds of 1 mm/s, 3 mm/s, and 5 mm/s. This phenomenon can be attributed to the fact that during low-speed extrusion, the heat generated by plastic deformation has more sufficient time to conduct and diffuse into the billet interior, resulting in a more uniform temperature distribution in the deformation zone. This, in turn, promotes more uniform and coordinated plastic flow of the material, ultimately leading to a more uniformly distributed equivalent strain.

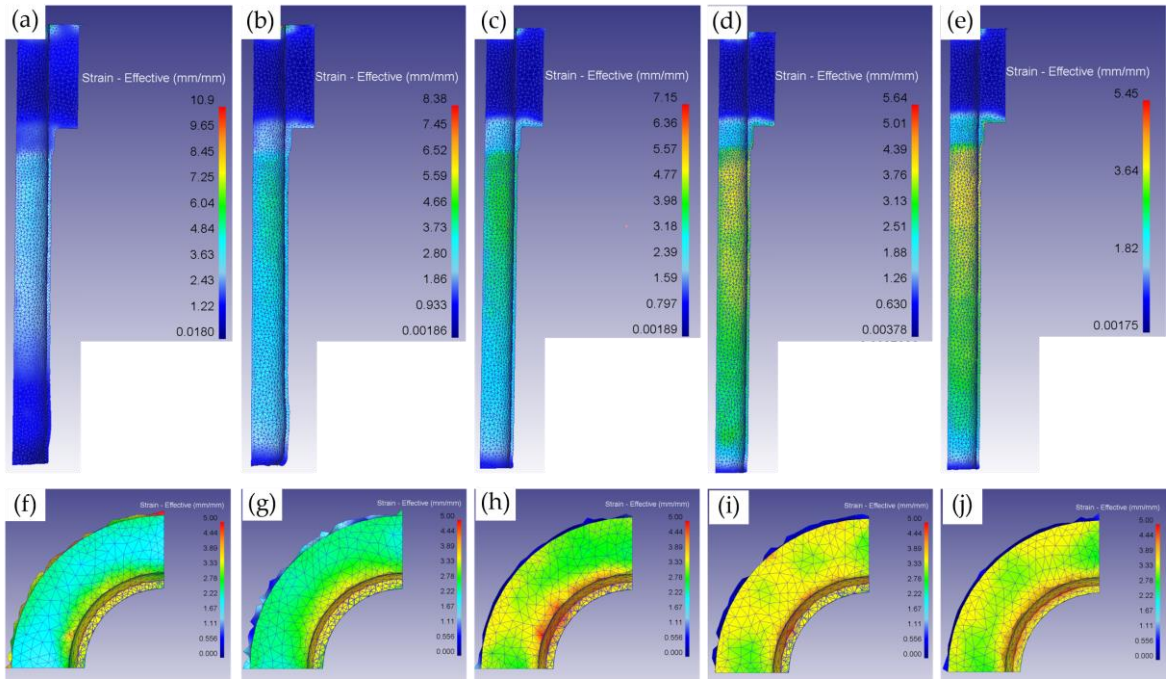


Figure 11. Effect of extrusion speed on extrusion equivalent strain.
Tube: (a) 0.1 mm/s; (b) 0.5 mm/s; (c) 1 mm/s; (d) 3 mm/s; (e) 5 mm/s
Die exit: (f) 0.1 mm/s; (g) 0.5 mm/s; (h) 1 mm/s; (i) 3 mm/s; (j) 5 mm/s

https://doi.org/10.64486/m.66.2.9

Figure 12 presents the effective strain and the effective strain deviation of the aluminum alloy tube at different extrusion speeds. The effective strain deviation is a dimensionless parameter that quantifies the uniformity of strain distribution across the tube cross-section; a lower deviation value indicates more homogeneous deformation and thus better forming quality. It can be observed from Figure 12 that at an extrusion speed of 0.5 mm/s, the average effective strain reaches its maximum value, while the effective strain deviation reaches its minimum of 1.4213. This indicates that under this condition, the strain distribution is the most uniform and the material undergoes the most sufficient plastic deformation. In summary, the best tube performance can be achieved at an extrusion speed of 0.5 mm/s.

To verify the reliability of the finite element simulation, backward extrusion experiments for the 7A60 aluminum alloy tube were conducted under the conditions of 390 °C and 0.5 mm/s. The extruded seamless tube is shown in Figure 13. The results indicated that under these forming conditions, the tube surface was free of cracks, and the material deformed stably and safely, demonstrating that the numerical simulation results provide a reliable reference for actual tube production.

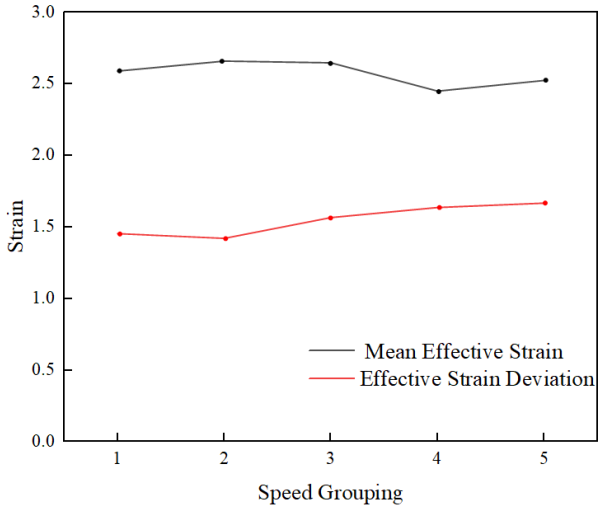


Figure 12. Average effective strain and effective strain deviation at different extrusion speeds

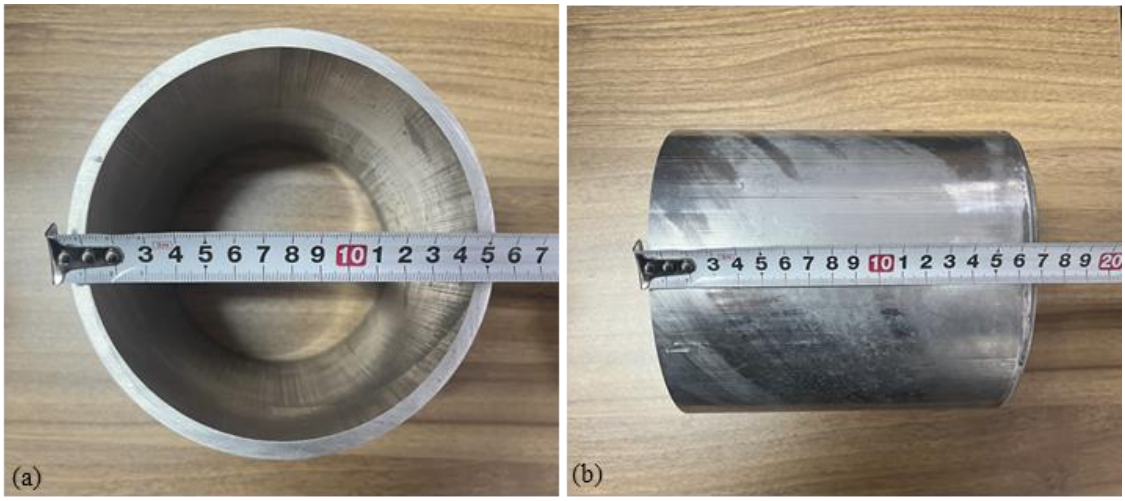


Figure 13. 7A60 aluminum alloy tube extruded product
(a) Perpendicular to the extrusion direction; (b) Extrusion direction

Based on a comprehensive analysis of the simulation results that considered strain uniformity, extrusion load, temperature distribution, and forming quality, the combination of 390 °C and 0.5 mm/s was identified as the optimal process parameters. The optimal extrusion temperature of 390 °C was determined based on three

https://doi.org/10.64486/m.66.2.9

considerations. First, this temperature yields the minimum effective strain deviation at this temperature (Figure 8), indicating the most uniform deformation. Second, the steady-state load of 6.48×10^3 kN at 390 °C provides a substantial reduction of 7.6 % compared to that at 360 °C while avoiding the overheating risks associated with higher temperatures. Third, the die-exit temperature of 414 °C at 390 °C remains within the safe processing window below the solidus, whereas higher preheating temperatures reduce the safety margin to the solidus temperature, with the die-exit temperature reaching 467 °C at 450 °C. The optimal extrusion speed of 0.5 mm/s was selected because it produces the maximum average effective strain combined with the minimum effective strain deviation of 1.4213 (Figure 12), it maintains an acceptable die-exit temperature of 414 °C that ensures stable forming without overheating, and it has been confirmed by experiments to yield defect-free products (Figure 13). In summary, 390 °C and 0.5 mm/s represent the optimal combination that balances deformation uniformity, forming load, temperature safety, and product quality.

To validate the reliability of the finite element model, the simulation results were compared with experimental measurements under the optimized condition of 390 °C and 0.5 mm/s. The comparisons are summarized in Table 4. The simulated and experimental results are in close agreement: the errors are 1.47 % for the die-exit temperature, 0.13 % for the outer diameter, and 0.84 % for the wall thickness. This demonstrates that the numerical model can accurately predict the extrusion process, and the validation confirms its reliability for process optimization. The extrusion force was not included in the quantitative validation due to the lack of independently recorded experimental data with sufficient precision. Nevertheless, the defect-free tubes produced under the optimized conditions confirm that the predicted forming load is practically feasible.

Table 4. Comparison between simulated and experimental results under the optimized condition (390 °C, 0.5 mm/s)

Parameter	Simulation	Experiment	Error
Die-exit temperature / °C	414	408	1.47 %
Tube outer diameter / mm	155.0	155.2	0.13 %
Tube wall thickness / mm	6.0	5.95	0.84 %

Figure 14 illustrates the microstructure evolution of the 7A60 aluminum alloy in the as-cast state, after homogenization treatment, and after backward extrusion. As shown in Figure 14(a), the as-cast alloy contains a large number of well-developed dendritic structures, with an average grain size of approximately 89 μm. After homogenization heat treatment, the dendritic characteristics are essentially eliminated, and the microstructure transforms into more regular equiaxed grains, with the average size reducing to about 74 μm (Figures 14b, c). This change is mainly attributed to the dissolution of the eutectic phase formed during non-equilibrium solidification during the prolonged high-temperature holding process, which promotes microstructure homogenization.

After the aluminum alloy billet undergoes backward extrusion, the cross-section of the tube exhibits a distinct layered structure from the surface inward, consisting sequentially of a fine-grained zone, a mixed-grain zone, and a fibrous structure elongated along the extrusion direction (Figures 14d–f). Specifically, the fine-grained zone is located on the outer side (red line area in Figure 14d) and the inner side (red line area in Figure 14f) of the tube, composed of fine equiaxed grains consistent with a dynamic recrystallization process. The mixed-grain zone is a transitional region where fine grains and fibrous grains coexist (yellow line areas in Figures 14d, f). The central part exhibits a typical fibrous deformed structure (Figure 14e) [19]. The reason for this gradient microstructure distribution lies mainly in the inhomogeneous strain and temperature fields during the extrusion process (as shown in Figures 5 and 7). The inner and outer sides of the tube, being in direct contact with the extrusion container and the mandrel, experience significant friction, leading to high local temperature rise and large strain. The higher strain energy and temperature jointly trigger dynamic recrystallization, thus forming the fine-grained zone. In the mixed-grain zone transitioning towards the center, where the thermal-

https://doi.org/10.64486/m.66.2.9

mechanical conditions are intermediate between the surface layers and the center, some grains undergo recrystallization to form fine grains, while the remaining grains retain their deformed fibrous characteristics due to insufficient driving force for recrystallization. In the central region of the tube, where temperature and strain are relatively low, the material primarily undergoes severe plastic flow. The original grains are significantly elongated and aligned directionally along the extrusion direction, ultimately forming a highly elongated fibrous structure [20].

It is noteworthy that the width of the outer fine-grained zone is approximately 189 μm, significantly larger than that of the inner fine-grained zone, which is about 89 μm. This difference primarily stems from the outer region experiencing greater deformation and stronger frictional effects from the die, which more significantly promotes the dynamic recrystallization process, causing more fibrous grains to transform into fine equiaxed grains [21].

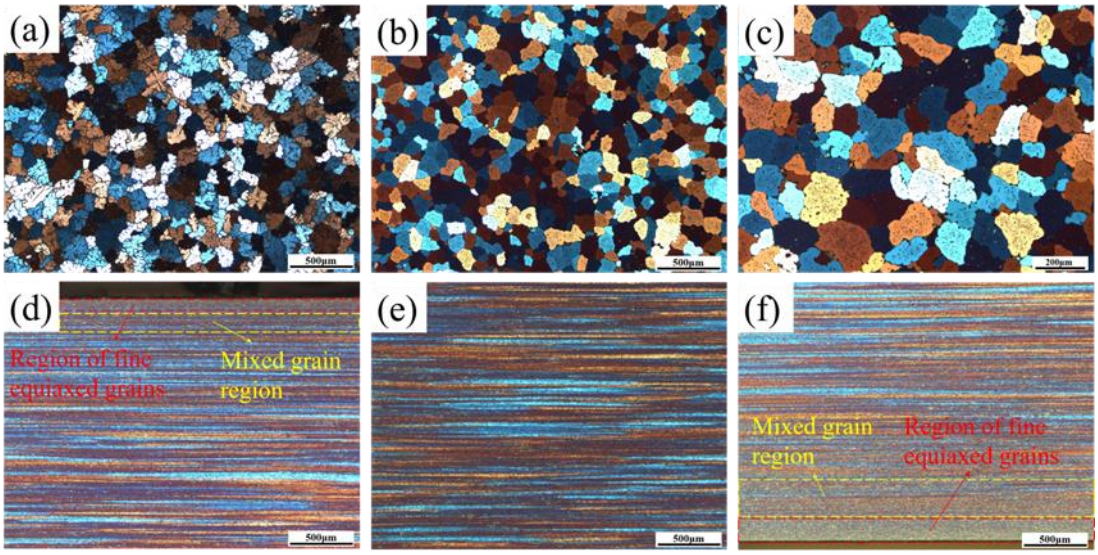


Figure 14. Microstructure of 7A60 aluminum alloy in as-cast, homogenized, and extruded states. (a) As-cast; (b)(c) Homogenized; (d)(e)(f) As-extruded outer side, central part, and inner side

Figure 15 shows the XRD patterns of the 7A60 aluminum alloy in the as-cast, homogenized, and extruded states. The analysis indicates that the alloy primarily consists of the α-Al matrix phase and the $MgZn_2$ phase. No diffraction peaks corresponding to the Al_2CuMg phase were detected in any of the treated states. Based on existing studies [22-24], this is mainly attributed to the Zn content in the alloy: when the Zn content exceeds 8 %, the transformation from the AlZnMgCu phase to the Al_2CuMg phase does not occur during homogenization, which explains the absence of this phase in the XRD patterns. Furthermore, compared to the as-cast and homogenized states, the diffraction peak intensity of the extruded alloy is significantly enhanced. This phenomenon is primarily due to the directional alignment of grains along the extrusion direction during the deformation process, resulting in the formation of a strong deformation texture, which enhances the diffraction intensity of specific crystallographic planes.

https://doi.org/10.64486/m.66.2.9

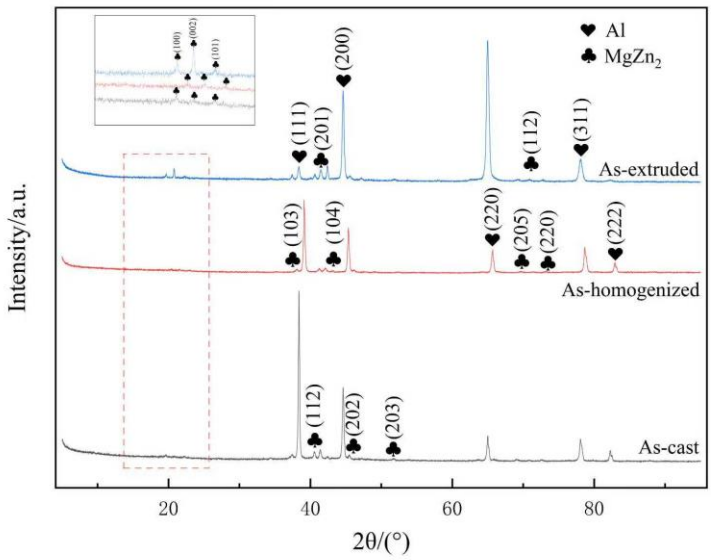


Figure 15. XRD analysis of 7A60 aluminum alloy in as-cast, homogenized, and extruded states

Figure 16 shows the secondary phase microstructure, EDS mapping distributions, and secondary phase area fraction statistics of the 7A60 aluminum alloy before and after extrusion, and Table 5 presents the EDS point analysis results for the 7A60 aluminum alloy in different states. Figure 16(a) displays the microstructure of the aluminum alloy in the as-cast state, where coarse and continuous network-like non-equilibrium eutectic structures are distributed within the aluminum matrix. EDS mapping results show that the primary solute elements Zn, Mg, and Cu are heavily enriched in these network-like bright white secondary phases distributed along the grain boundaries, with a small amount of Fe element also distributed. The degree of elemental inhomogeneity follows the order Cu > Zn > Mg > Fe. Combined with the point scan analysis in Table 5, the network-like bright white phase is tentatively identified as a mixture of α-Al and AlZnMgCu phases, and the bright white granular secondary phase is tentatively identified as the Al_7Cu_2Fe phase. These assignments are based on EDS compositional analysis and are supported by previous studies on similar 7xxx series aluminum alloys [22-24]. Meanwhile, the area fraction of secondary phases in the alloy reaches its highest value of 5.5 % (Figure 16(f)).

Figure 16(b) shows the microstructure morphology of the aluminum alloy after homogenization treatment. After high-temperature treatment, the secondary phases in the as-cast structure are fragmented and partially dissolved back into the aluminum matrix. The distribution of Zn, Mg, and Cu elements in the matrix becomes more uniform and dispersed compared to the as-cast state, no longer exhibiting obvious network-like enrichment characteristics, and the elemental segregation is significantly improved. At this stage, the morphology of the secondary phases in the structure gradually transforms from a continuous network structure into residual coarse blocky AlZnMgCu phases, dispersedly distributed granular and strip-like $MgZn_2$ phases, and a small amount of bright white Fe-rich phases (Al_7Cu_2Fe). Statistical results show that the area fraction of secondary phases slightly decreases to 5.2 % after homogenization. This is because some incompletely dissolved AlZnMgCu phases and highly thermally stable Fe-containing impurity phases (Al7Cu2Fe) still remain in the structure, limiting further reduction in the total secondary phase content.

Figures 16(c), (d), and (e) show the SEM microstructures of the inner side, central part, and outer side of the aluminum alloy tube in the extruded state, respectively. It can be clearly seen from the figures that, under the combined effect of high temperature and severe shear deformation, the coarse secondary phases remaining after homogenization are mechanically broken and distributed in an intermittent chain-like pattern along the extrusion direction. According to points E to I, the secondary phases in the aluminum alloy tube mainly consist of broken white blocky AlZnMgCu phases, elongated strip-like and granular $MgZn_2$ phases dispersedly

https://doi.org/10.64486/m.66.2.9

distributed in the aluminum matrix, and a small amount of Al_7Cu_2Fe impurity phases that still appear bright white. From Figures 16(c), (d), and (e), it is evident that the fragmentation and elongation of secondary phases at the edges of the tube are more significant compared to the central part. The statistical results in Figure 16(f) further confirm this phenomenon: the area fractions of secondary phases in the inner side, central part, and outer side are 3.8 %, 4.9 %, and 3.4 %, respectively. This is because the edge regions of the tube experience strong friction and shear from the die during extrusion, resulting in the greatest degree of deformation. This leads to more thorough fragmentation and refinement of coarse secondary phase particles, and the temperature rise generated by severe deformation promotes further dissolution of the secondary phases, thereby significantly reducing the residual secondary phase content. In contrast, the central part is in a relatively low-deformation zone for metal flow, experiencing less shear stress. The degree of fragmentation and dissolution of secondary phases is not as significant as in the edge regions, thus retaining a higher proportion of secondary phase particles.

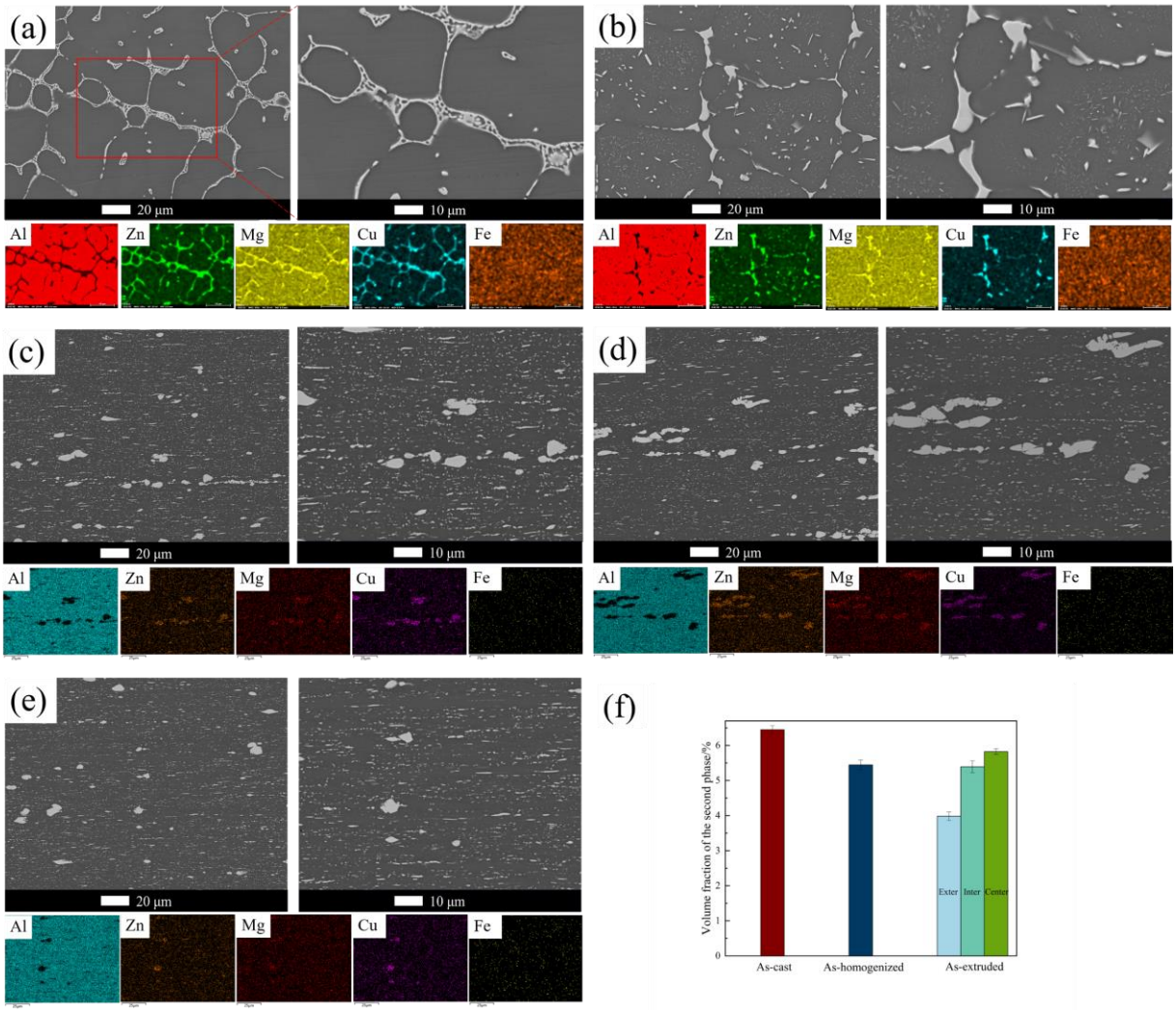


Figure 16. SEM microstructure and secondary phase area fraction of 7A60 aluminum alloy in as-cast, homogenized, and extruded states. (a) As-cast; (b) Homogenized; (c)(d)(e) As-extruded inner side, central part, and outer side; (f) Secondary phase area fraction

Figure 17 shows the columnar statistical chart of the room-temperature tensile properties of the 7A60 aluminum alloy in the as-cast, homogenized, and extruded states. It can be seen from the figure that in the as-cast state, the aluminum alloy exhibited a yield strength of 194.2 MPa, an average ultimate tensile strength of 287.5 MPa, and an elongation of 7.8 %. The mechanical properties were the poorest at this stage, which is attributed to the presence of numerous well-developed dendrites and coarse continuous network-like non-

https://doi.org/10.64486/m.66.2.9

equilibrium eutectic structures distributed along the grain boundaries in the as-cast microstructure (Figure 14a, Figure 15a). These brittle phases readily act as crack initiation sites under stress. In the homogenized state of the aluminum alloy extrusion billet, the yield strength was 235.6 MPa, the average ultimate tensile strength was 316.2 MPa, and the elongation was 15.3 %. This improvement is because the homogenization treatment essentially eliminated dendritic segregation, transforming the grains into equiaxed grains and reducing stress concentration sources. After extrusion deformation, the aluminum alloy tube achieved a yield strength of 272 MPa, an average ultimate tensile strength of 426.8 MPa, and an elongation of 14.0 %. The reasons for the enhanced mechanical properties are as follows: during extrusion, the alloy underwent dynamic recrystallization, forming fine equiaxed grain zones at the edges of the tube. The increase in grain boundary area effectively impeded dislocation motion, providing a fine-grain strengthening effect. Additionally, the residual coarse secondary phases were mechanically broken into fine particles, which pinned dislocations. Simultaneously, the extrusion deformation introduced a high density of dislocations and a fibrous deformation texture along the extrusion direction, resulting in a significant work hardening effect.

Table **5**. EDS point analysis results of 7A60 aluminum alloy in different states

Location	Element compositions, at%					Probable Phases
	Al	Zn	Mg	Cu	Fe	
A	59.82	15.95	17.39	6.79	0.04	α-Al+AlZnMgCu
B	55.85	16.78	15.10	9.10	3.16	Al_7Cu_2Fe
C	63.55	19.32	12.29	4.84	—	$MgZn_2$
D	28.14	26.37	32.64	12.78	0.07	AlZnMgCu
E	21.50	28.77	32.13	17.54	0.06	AlZnMgCu
F	70.60	13.53	10.41	5.46	—	$MgZn_2$
G	78.51	10.64	7.86	2.99	—	$MgZn_2$
H	78.06	10.36	7.91	3.68	—	$MgZn_2$
I	77.53	3.09	1.51	11.95	5.92	Al_7Cu_2Fe

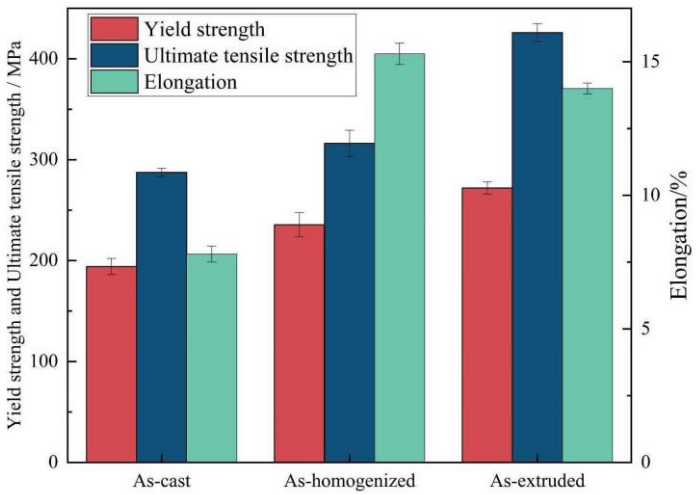


Figure 17. Room-temperature tensile properties of 7A60 aluminum alloy in as-cast, homogenized, and extruded states. Error bars represent the standard deviation calculated from three replicate tensile tests. All tensile specimens were machined parallel to the extrusion direction

https://doi.org/10.64486/m.66.2.9

4. Conclusions

(1) Extrusion temperature and speed significantly affect the forming quality of 7A60 aluminum alloy tubes. When the extrusion temperature increased from 360 °C to 450 °C, the average steady-state load decreased by 24.0 %, and the maximum equivalent stress decreased by 16.1 %. However, excessively high temperatures could easily lead to overheating at the die exit, increasing the risk of hot cracks. Increasing the speed intensified the temperature rise; when the speed reached ≥3 mm/s, the exit temperature reached (492–516) °C, exceeding the alloy's solidus line. The equivalent stress showed a trend of first decreasing and then increasing, while strain uniformity decreased. The optimal process parameters were comprehensively determined to be 390 °C and 0.5 mm/s, under which the effective strain deviation was minimal (1.4213) and the forming quality was optimal.

(2) After extrusion, the tube exhibited a distinct layered microstructure: an outer fine-grained zone consistent with dynamic recrystallization (width 189 μm), an inner fine-grained zone (width 89 μm), a central fibrous structure, and a mixed-grain transition zone. Coarse secondary phases were broken and distributed along the extrusion direction. The area fraction of secondary phases decreased from 5.5 % in the as-cast state to 3.4 % (outer side) and 4.9 % (center) in the extruded state, with the degree of fragmentation and dissolution at the edges being superior to that in the center.

(3) The reasonable backward extrusion process significantly enhanced the mechanical properties. The ultimate tensile strength increased from 287.5 MPa (as-cast) to 426.8 MPa, the yield strength increased from 194.2 MPa to 272 MPa, and the elongation increased from 7.8 % to 14.0 %. The improvement in properties was attributed to the synergistic effects of fine-grain strengthening, secondary phase dispersion strengthening, and work hardening.

Acknowledgments: This work was supported by the Innovation and Development Project of Basic Scientific Research for Higher Education Institutions from the Department of Education of Liaoning Province (LJ242510146002) and the Natural Science Foundation of China (No. 52104377).

References

[1] X. Y. Huang and B. Liu, "Light alloy is first choice metal materials for weapon equipment lightweighting," *Light Alloy Fabrication Technology*, vol. 2007, no. 1, pp. 12-15, 2007. (in chinese).

[2] Q. W. Ding, D. Zhang, J. R. Zuo, S. L. Hou, L. Z. Zhuang, and J. S. Zhang, "The effect of grain boundary character evolution on the intergranular corrosion behavior of advanced Al-Mg-3wt%Zn alloy with Mg variation," *Materials Characterization*, vol. 146, pp. 47-54, 2018, https://doi.org/10.1016/j.matchar.2018.09.044

[3] W. K. Krajewski, J. Buraś, P. K. Krajewski, A. L. Greer, K. Faerber, and P. Schumacher, "New Developments of Al-Zn Cast Alloys," *Materials Today: Proceedings*, vol. 2, no. 10, pp. 4978-4983, 2015, https://doi.org/10.1016/j.matpr.2015.10.078

[4] Y. J. Wang, Y. Jia, S. Z. Zhang, S. Z. Cao, S. L. Zhang, W. Zhang, C. Z. Zhang, Z. P. Hou, J. C. Han, and T. Wang, "Comprehensive evaluation of the effect of large extrusion ratio on the microstructure and performance of Al/Al bimetallic composite tubes," *Journal of Materials Processing Technology*, vol. 338, pp. 118783, 2025, https://doi.org/10.1016/j.jmatprotec.2025.118783

[5] L. Li, H. Zhang, J. Zhou, J. Duszczyk, G. Y. Li, and Z. H. Zhong, "Numerical and experimental study on the extrusion through a porthole die to produce a hollow magnesium profile with longitudinal weld seams," *Materials & Design*, vol. 29, no. 6, pp. 1190-1198, 2007, https://doi.org/10.1016/j.matdes.2007.05.003

[6] W. S. Chen, M. Q. Luo, and J. A. Liu, "Reverse Extrusion Characteristics for Aluminum Alloy and Development Prospect in China," *Aluminum Fabrication*, no. 2, 2016, pp. 42-44, 2016. (in chinese).

[7] J. S. Qiao, Y. J. Li, X. B. Zhang, and Q. L. Li, "Preparation and microstructure evolution analysis of bimetallic aluminum alloy composite tubes by indirect extrusion," *Journal of Plasticity Engineering*, vol. 32, no. 1, pp. 49-58, 2025. (in chinese).

[8] X. W. Yang, J. C. Zhu, Z. H. Lai, Y. Liu, D. He, and Z. S. Nong, "Finite element analysis of quenching temperature field, residual stress and distortion in A357 aluminum alloy large complicated thin-wall workpieces," *Transactions of Nonferrous Metals Society of China*, vol. 23, no. 6, pp. 1751-1760, 2013, https://doi.org/10.1016/S1003-6326(13)62657-6

[9] F. Li, J. F. Lin, C. Li, and X. J. Liu, "Optimization based on extrusion for seamless tube of super hardness aluminum alloy," *Journal of Central South University (Science and Technology)*, vol. 42, no. 10, pp. 3020-3025, 2011. (in chinese).

 https://doi.org/10.64486/m.66.2.9

[10] Y. Zhang, Q. Liang, C. Y. Xiao, S. L. Zheng, and Y. Tang, "Numerical Simulation and Analysis of Extrusion Forming Process of Aluminum Alloy Seamless Tube," Journal of Hunan Institute of Science and Technology (Natural Sciences), vol. 34, no. 1, pp. 50-56, 2021. (in chinese).

[11] M. Ketabchi, H. Mohammadi, and M. Izadi, "Finite-Element Simulation and Experimental Investigation of Isothermal Backward Extrusion of 7075 Al Alloy," *Arabian Journal for Science and Engineering*, vol. 37, pp. 2287-2296, 2012, https://doi.org/10.1007/s13369-012-0320-4

[12] A. Neag, V. Favier, L. Nistor, and R. Bigot, "Numerical Simulation and Experimental Investigation on Thixo-Backward Extrusion of 7075 Aluminium Alloy," *Advanced Engineering Forum*, no. 8-9, pp. 269-276, 2013, https://doi.org/10.4028/www.scientific.net/AEF.8-9.269

[13] S. Q. Wang, H. Liu, Z. Q. Chen, H. L. Wang, Z. Q. Li, and L. Chen, "Numerical simulation on extrusion forming for large ribbed thin-walled circular tube aluminum profile," *Forging & Stamping Technology*, vol. 47, no. 4, pp. 181-189, 2022. (in chinese).

[14] K. M. Xue, D. Q. Bo, and P. Li, "Hot compression microstructure and rheological behavior of rolled 7A60 aluminum alloy," *Materials Review B: Research Papers*, vol. 32, no. 4, pp. 1306-1310, 2018. (in chinese).

[15] H. X. Niu, G. Q. Gan, P. Li, and K. M. Xue, "Finite Element Simulation and Experimental Verification of Semi-solid Forming of 7075 Aluminum Alloy Cylinder Based on DEFORM-3D," *Rare Metal Materials and Engineering*, vol. 51, no. 5, pp. 1697-1704, 2022. (in chinese).

[16] H. T. Yang, Z. Lu, and J. L. Gu, "Study on the Flow Stress of 7A60 Ultra High Strength Aluminum Alloy," *Journal of Aeronautical Materials*, vol. 2005, no. 2, pp. 12-15, 2005. (in chinese).

[17] B. Zhao, P. Li, J. L. Wang, and K. M. Xue, "Microstructure evolution and element distribution of semi-solid 7A60 aluminum," *Journal of Plasticity Engineering*, vol. 23, no. 5, pp. 160-167, 2016. (in chinese).

[18] H. Liu, J. W. Tang, J. H. Cao, D. H. Wang, Y. L. Fu, S. H. Wang, and L. Chen, "Numerical simulation and experimental study on backward extrusion process for a novel high strength and toughness 7A99 aluminum alloy," *Forging & Stamping Technology*, vol. 50, no. 10, pp. 125-134, 2025. (in chinese).

[19] Y. Birol and O. Ilgaz, "Effect of cast and extruded stock on grain structure of EN AW 6082 alloy forgings," *Materials Science and Technology*, vol. 30, no. 7, pp. 860-866, 2014, https://doi.org/10.1179/1743284713Y.0000000407

[20] N. Marco, P. Riccardo, D. Lorenzo, and R. Barbara, "Numerical investigation of the surface recrystallization during the extrusion of a AA6082 aluminum alloy under different process conditions," *The International Journal of Advanced Manufacturing Technology*, vol. 129, no. 3-4, pp. 1585-1599, 2023, https://doi.org/10.1007/S00170-023-12397-8

[21] S. Y. Tian, X. M. Zang, Z. M. Liu, T. Z. Jia, Z. Xu, and Z. H. Zhao, "Comparative Analysis of Microstructure and Mechanical Properties in Aluminum Alloy Automotive Control Arms Fabricated from Extruded Bars versus Horizontal Direct Chill Cast Bars," *Materials Transactions*, vol. 66, no. 12, pp. 1531-1538, 2025, https://doi.org/10.2320/MATERTRANS.MT-M2025110

[22] K. Wen, B. Q. Xiong, Y. A. Zhang, G. J. Wang, X. W. Liu, Z. H. Li, S. H. Huang, and H. W. Liu, "Microstructure Evolution of a High Zinc Containing Al-Zn-Mg-Cu Alloy during Homogenization," Rare Metal Materials and Engineering, vol. 46, no. 4, pp. 928-934, 2017, https://doi.org/10.1016/S1875-5372(17)30124-8

[23] R. S. Huang, H. F. Yang, S. J. Zheng, M. N. Li, H. Wang, Y. H. Duan, C. F. Yue, and C. Yang, "The evolution mechanism of the second phase during homogenization of Al-Zn-Mg-Cu aluminum alloy," Materials & Design, vol. 235, pp. 112395, 2023, https://doi.org/10.1016/J.MATDES.2023.112395

[24] F. B. Guo, B. H. Zhu, L. B. Jin, G. J. Wang, H. W. Yan, Z. H. Li, Y. A. Zhang, and B. Q. Xiong, "Microstructure and mechanical properties of 7A56 aluminum alloy after solution treatment," Rare Metals, vol. 40, pp. 168-175, 2021, https://doi.org/10.1007/s12598-017-0985-7

https://doi.org/10.64486/m.66.2.9